The Astrophysical Journal Letters, 901:L36 (8pp), 2020 October 1 https://doi.org/10.3847/2041-8213/abb87f

How Does Background Air Pressure Influence the Inner Edge of the Habitable Zone for Tidally Locked Planets in a 3D View?

Yixiao Zhang and Jun Yang
Dept. of Atmospheric and Oceanic Sciences, School of Physics, Peking University, Beijing 100871, People's Republic of China; junyang@pku.edu.cn
Received 2020 July 31; revised 2020 September 13; accepted 2020 September 14; published 2020 October 1

Abstract

We examine the effect of varying background N_2 surface pressure (labeled as pN_2) on the inner edge of the habitable zone for 1:1 tidally locked planets around M dwarfs, using the three-dimensional (3D) atmospheric general circulation model (AGCM) ExoCAM. In our experiments, the rotation period is fixed when varying the stellar flux, in order to more clearly isolate the role of pN_2. We find that the stellar flux threshold for the runaway greenhouse is a non-monotonous function of pN_2. This is due to the competing effects of five processes: pressure broadening, heat capacity, lapse rate, relative humidity, and clouds. These competing processes increase the complexity in predicting the location of the inner edge of the habitable zone. For a slow-rotation orbit of 60 Earth days, the critical stellar flux for the runaway greenhouse onset is 1700–1750, 1900–1950, and 1750–1800 W m^{-2} under 0.25, 1.0, and 4.0 bar of pN_2, respectively, suggesting that the magnitude of the effect of pN_2 is within ≈13%. For a rapid rotation orbit, the effect of varying pN_2 on the inner edge is smaller, within a range of ≈7%. Moreover, we show that Rayleigh scattering effect as varying pN_2 is unimportant for the inner edge due to the masking effect of cloud scattering and to the strong shortwave absorption by water vapor under hot climates. Future work using AGCMs having different cloud and convection schemes and cloud-resolving models having explicit cloud and convection are Required to revise this problem.

Unified Astronomy Thesaurus concepts: Exoplanet atmospheres (487); Planetary atmospheres (1244); Extrasolar rocky planets (511); Astrobiology (74); Habitable planets (695)

1. Introduction

Various factors can influence the width of the habitable zone around stars, including stellar spectrum, planetary rotation, radius and gravity, orbital obliquity and eccentricity, air mass and composition, surface land and sea configurations, etc. (Kasting et al. 1993, 2014; Selsis et al. 2007; Pierrehumbert 2010; Leconte et al. 2013; Yang et al. 2013, 2014a, 2019a; Zsom et al. 2013; Wolf & Toon 2014, 2015; Wordsworth 2015; Kopparapu et al. 2016, 2017; Shields et al. 2016; Wang et al. 2016; Wolf et al. 2017; Bin et al. 2018; Way et al. 2018; Ramirez 2020). In this study, we investigate the effect of varying pN_2. N_2 is a common atmospheric composition of rocky planets in the solar system. The value of pN_2 is 0.78 bar on modern Earth, less than 0.5 bar on early Earth (Marty et al. 2013; Som et al. 2016), 1.4 bar on Titan (≈10 times Earth's value for per unit area, given Titan's gravity is only 1.35 m s^{-2}), and 3.3 bar on Venus (Ingersoll 2013). Planets beyond the solar system are expected to also have a wide range of pN_2, which is determined by many processes such as accretion from the protoplanetary disk, impacts, lightning, volcanism, atmospheric escape, photochemistry, and ocean chemistry (Johnson & Goldblatt 2015; Wordsworth 2016; Hu & Diaz 2019).

Although N_2 is not a greenhouse gas, it can influence planetary climate through several processes, including pressure broadening (as well as collision-induced N_2–N_2 continuum absorption, warming effect; Figure 1(a)), Rayleigh scattering (cooling effect; Figure 1(b)), heat capacity, lapse rate (i.e., the vertical profile of air temperature), and energy transport. The relative importance of these effects depends on the level of pN_2 and the climate state. For temperate climates of early Earth and early Mars for which pN_2 is not very high, the warming effect of pressure broadening dominates (Goldblatt et al. 2009; Charnay et al. 2013; von Paris et al. 2013; Wolf & Toon 2014). For temperate or cold climate with high-level pN_2 but relatively low greenhouse gases (such as H_2O and CO_2), the cooling effect of Rayleigh scattering dominates (Keles et al. 2018). Moist adiabatic lapse rate ($-\partial T/\partial z$) increases with pN_2 (Figure 1(d)), which influences vapor concentration aloft (Figure 1(e)), strength of the greenhouse effect (Nakajima et al. 1992; Pierrehumbert 2010), and shortwave heating rate (Figure 1(f)). Atmospheric heat capacity ($C_p dm$, where C_p is the specific heat capacity and dm is the air mass per unit area between two adjacent vertical levels) increases with pN_2, which can also strongly affect shortwave heating rate, longwave cooling rate, and condensation heating rate (Chemke et al. 2016). As shown in Figure 1(f), the shortwave heating rate ($=F_{SW}/(C_p dm)$, where F_{SW} is the net shortwave flux for each level) decreases significantly with pN_2 due to the decrease of water vapor aloft and the increase of heat capacity. The magnitude of pN_2 can also influence horizontal and vertical energy transports (Kaspi & Showman 2015; Chemke et al. 2016; Chemke & Kaspi 2017; Komacek & Abbot 2019). In this work, we examine the net effect of pN_2 on the inner edge of the habitable zone with a model including all these processes as well as clouds and atmospheric subsaturation.

Following Kasting et al. (1993), the inner edge is defined as the location where absorbed shortwave radiation of the planet exceeds the upper limit of outgoing longwave radiation at the top of the atmosphere (OLR_m) where the entire ocean would evaporate. The onset of a moist greenhouse state (i.e., high water vapor concentration above the tropopause and significant water loss to space; see Wordsworth & Pierrehumbert 2014) will not be considered in this study, because the work of Kopparapu et al. (2017) and Fujii et al. (2017) showed that slow-rotation tidally locked planets around low-mass stars can undergo water loss but remain habitable. Moreover, for water-

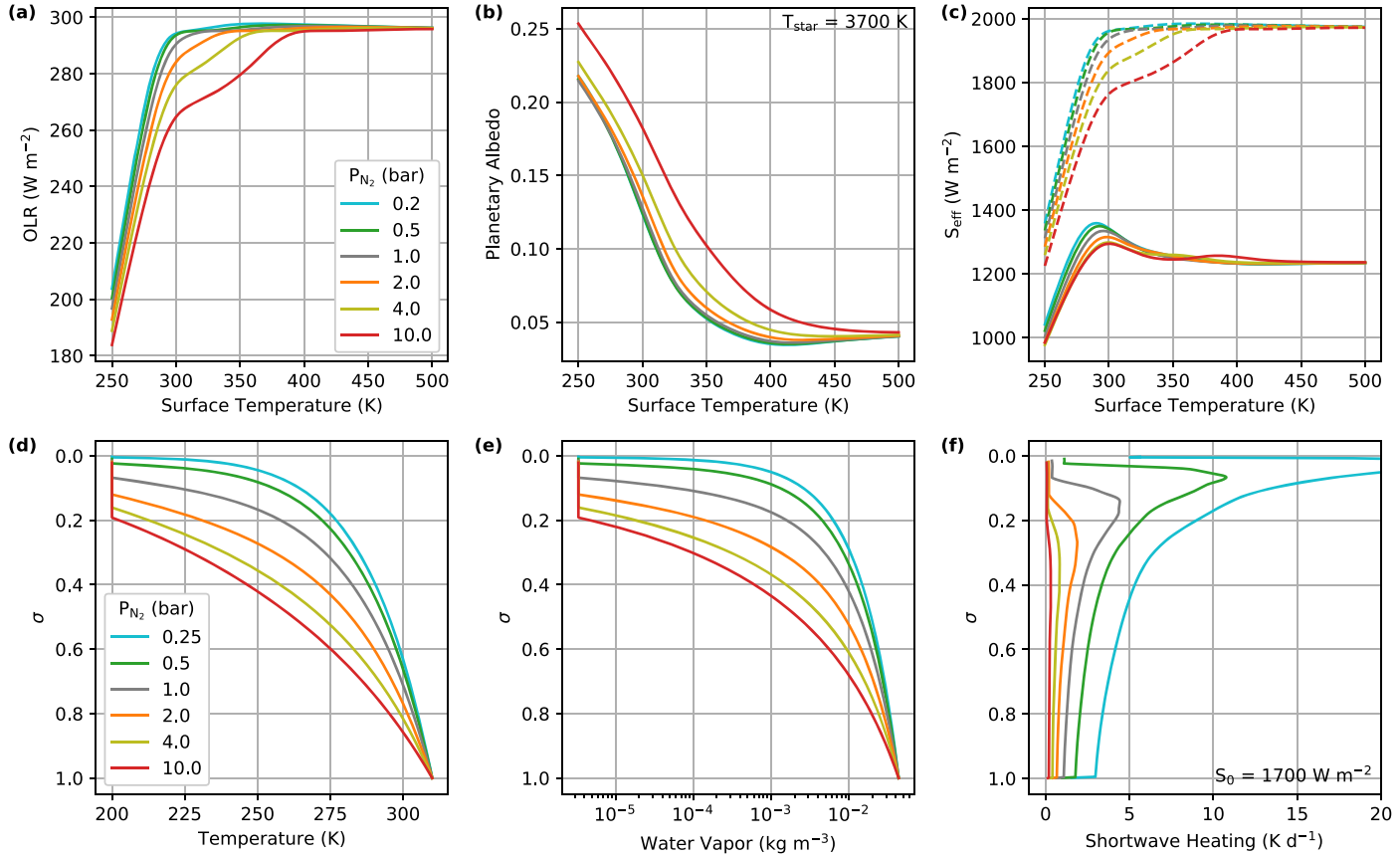

Figure 1. Effects of different pN_2 on radiation transfer, calculated using the 1D radiative-convective model ExoRT. (a)–(c) The effects of pN_2on outgoing longwave radiation (a, OLR), planetary albedo (b, α_p), and the effective stellar flux (defined as $(4 \times \mathrm{OLR})/(1 - \alpha_p)$, which is the stellar flux required to maintain a given surface temperature; the dashed lines show the results under an assumed α_p of 0.4), as a function of surface temperature from 250 to 500 K. (d)–(f) Vertical profiles of air temperature in σ-coordinates under a fixed surface temperature of 310 K (d), water vapor density (e), and calculated shortwave heating rate (f). In these calculations, stellar flux is 1700 W m^{-2}, star temperature is 3700 K, solar zenith angle is 60°, surface albedo is 0.25, and no cloud is included. The air temperature decreases from the surface to the top following moist adiabatic profile until it reaches 200 K, above which the atmosphere is isothermal with a constant water mixing ratio (see Kasting et al. 1993). The decreasing of shortwave heating rate with pN_2 in (f) is due to the combined effect of the reduction of water vapor aloft and the increase of heat capacity; the effect of heat capacity dominates.

rich planets, only a fraction of the ocean may be lost within the lifetime of the planets, so water loss in moist greenhouse state is not a ultimate threat for planetary habitability (Selsis et al. 2007; Moore & Cowan 2020). Here, we focus on the runaway greenhouse.

Using 1D radiative-convective model, Kasting et al. (1993) showed that varying pN_2 has an insignificant effect on the runaway greenhouse limit (see their Table 2). This is due to that for the runaway greenhouse state the atmosphere is dominated by water vapor and the presence of N_2 is not so important. Studies with updated absorption coefficients for CO_2 and H_2O found that varying pN_2 has an effect of within ≈10% on the runaway greenhouse limit (Figure 4.38 in Pierrehumbert 2010; Figure 5 in Goldblatt et al. 2013; Figure 1(a) in Kopparapu et al. 2014; and see also Figure 1(c) here), due to the combined effects of pressure broadening, lapse rate, and Rayleigh scattering. Ramirez (2020) further showed that the effect of pN_2 for M and K dwarfs is much weaker than that for F and A stars, due to the lower Rayleigh scattering and higher near-infrared absorption of water vapor under redder spectra. Vladilo et al. (2013) and Zsom et al. (2013) found that the effect of pN_2 on the inner edge could be as large as 65% in 1D climate calculations; however, they used the boiling point as the inner edge (this is unconventional in literature), and meanwhile they employed a relative humidity of 1% or 50% rather than 100% that is always assumed in 1D radiative-convective models.

Two weaknesses of the 1D models are that clouds are not simulated and relative humidity is fixed, because clouds and humidity are primarily determined by 3D atmospheric circulation and convection. In this study, we plan to improve the understanding of this problem through 3D simulations with an atmospheric general circulation model (AGCM; Section 2). We focus on tidally locked planets around M dwarfs due to their relatively large planet-to-star ratio and frequent transits. Previous 3D experiments have been employed to examine the inner edge for tidally locked planets (such as Yang et al. 2013, 2014a, 2019c, 2019d; Kopparapu et al. 2016, 2017; Way et al. 2016; Bin et al. 2018), but these studies always assumed pN_2 being equal to ≈1.0 bar. Below, we show that the magnitude of varying pN_2 on the runaway greenhouse limit is within ≈13%, similar to that found in 1D radiative-convective models, but the underlying mechanisms are different and more complex than those found in 1D models. More important, we find that the dependence of the inner edge on pN_2 is non-monotonic, especially for a slow-rotation orbit (Section 3). A summary is given in Section 4.

Table 1

Global-mean Surface Temperature (T_s), Energy Balance at the Top of the Atmosphere (Net Shortwave minus Net Longwave, Labeled as EB), Planetary Albedo (α_p), Surface Albedo (α_s), Vertically Integrated Water Vapor (Q), Clear-sky Greenhouse Effect (G_c), Longwave Cloud Radiation Effect (LWCRE), and Shortwave Cloud Radiation Effect (SWCRE) under Different Stellar Temperatures (T_{star}), Rotation Periods (P), Surface N_2 Pressures (pN_2), and Stellar Fluxes (S_0), Simulated with ExoCAM

T_{star} (K)	P (days)	pN_2 (bar)	S_0 (W m^{-2})	T_s (K)	EB (W m^{-2})	α_p (0–1)	α_s (0–1)	Q (kg m^{-2})	G_c (K)	LWCRE (W m^{-2})	SWCRE (W m^{-2})
3700	60	0.25	1600	269.3	−2.0	0.39	0.08	42.6	7.8	21.4	−131.4
			1700	277.6	−0.3	0.40	0.06	63.7	12.0	28.5	−150.8
			1750	326.0 (runaway)	70.9	0.19	0.05	1536.0	50.5	34.4	−72.2
		0.5	1700	265.8	−1.8	0.43	0.11	37.6	7.1	17.2	−159.1
		1.0	1600	258.9	−1.5	0.44	0.16	26.7	5.1	16.4	−147.3
			1700	264.8	−1.0	0.44	0.13	37.2	7.4	15.3	−161.4
			1750	270.3	−0.5	0.44	0.09	49.2	10.0	19.5	−170.5
			1800	278.9	0.4	0.44	0.07	74.3	14.9	25.6	−176.3
			1900	312.1	0.8	0.44	0.07	325.8	41.8	34.8	−189.3
			1950	383.6 (runaway)	114.0	0.05	0.05	10565.5	93.8	42.1	−11.7
		2.0	1700	278.2	−0.6	0.41	0.07	67.2	15.9	22.3	−153.1
		4.0	1600	282.7	−0.1	0.38	0.07	72.5	20.6	22.4	−124.4
			1700	296.7	0.4	0.38	0.07	137.4	31.0	22.9	−137.0
			1750	308.7	−0.9	0.40	0.07	218.4	41.6	24.1	−147.6
			1800	371.5 (runaway)	9.1	0.37	0.06	7480.4	107.6	39.8	−149.4
		10.0	1700	343.9	−0.1	0.38	0.06	752.1	77.1	22.3	−126.9
2600	6	0.25	1200	256.1	−3.7	0.24	0.14	32.2	5.2	11.7	−44.6
			1300	274.8	−1.1	0.19	0.07	91.5	11.2	22.7	−48.5
			1350	336.4 (runaway)	19.1	0.09	0.04	1589.6	59.4	34.2	−25.3
		1.0	1200	259.3	−1.8	0.23	0.14	25.6	6.4	12.7	−49.7
			1300	277.8	−0.9	0.17	0.07	69.4	13.5	17.2	−45.8
			1350	289.6	0.1	0.14	0.06	157.3	19.9	19.4	−38.6
			1400	363.7 (runaway)	24.6	0.06	0.05	4885.7	85.1	85.1	−17.3
		4.0	1200	262.6	−2.1	0.21	0.16	16.3	9.5	6.1	−43.4
			1400	310.6	0.2	0.12	0.05	175.6	37.4	13.0	−32.7
			1450	359.3 (runaway)	6.6	0.06	0.06	2599.9	79.8	14.5	−19.4

Note. Averages of the last 10 model (Earth) years in each experiment are shown, except in the runaway greenhouse state (red color) averages of the last 1 model year before model crash are listed.

2. Methods

The AGCM used in this study is ExoCAM. The model is based on the Community Atmospheric Model version 4 but modified by Eric Wolf for simulating early Earth and terrestrial exoplanets (Wolf & Toon 2014, 2015; Wolf 2017; Wolf et al. 2017). Two main modifications are the radiation transfer for high concentrations of CO_2 and H_2O and the numerical solver for entropy calculation within the Zhang–MacFarlane convection parameterization, so that ExoCAM is able to well simulate the onset of runaway greenhouse. In the model, correlated-k coefficients are based on the database of HITRAN 2012, and water vapor continuum absorption and collision-induced N_2–N_2 absorption are included.

Atmospheric compositions are set to Earth-like, including N_2 and H_2O, but O_2, O_3, CO_2, CH_4, and aerosols are not considered. The total pressure of the atmosphere is given by $P_{tot} = pN_2 + pH_2O$. Several different surface pN_2 were examined, from 0.25 to 10 bar (Table 1). Planetary radius and gravity are the same as Earth. Two different rotation periods are tested, 60 and 6 Earth days. All the experiments are set to be 1:1 tidally locked, i.e., rotation period = orbital period. The stellar temperature is 3700 K for the slow-rotation orbit and 2600 K for the rapid rotation orbit. Stellar spectra are from the BT_Settl stellar model (Allard et al. 2007). A series of stellar flux were examined with an interval of 50 or 100 W m^{-2} (Table 1). Our experimental design is different from that employed in Kopparapu et al. (2016, 2017), who modified the rotation period and the stellar flux simultaneously. Their experiments are able to self-consistently consider the combined effect of the Coriolis force and stellar flux, but do not allow separate considerations of each factor. In our simulations, the rotation period is fixed when varying the stellar flux, as was done by such as Merlis & Schneider (2010), Way et al. (2016), Noda et al. (2017), and Bin et al. (2018). This design allows us to isolate the effect of stellar radiation, and it is sufficient to demonstrate the role of varying air pressure. Future work is required to consistently investigate the combined effect of varying the rotation rate and stellar flux.

The atmosphere is coupled to an immobile, slab ocean with a depth of 50 m and with no oceanic dynamics; no continent is considered. Previous studies have shown that oceanic heat transport (OHT) is important for the planets in the middle range of the habitable zone, but its magnitude is much smaller for planets close to the inner edge (Yang et al. 2019b). The latter is due to that under hot climates, temperature contrasts between dayside and nightside are small and thereby surface winds are

weak. Sea ice is allowed to form when the surface temperature is below the freezing point (271.35 K), and the albedos of sea ice and snow depend on the stellar spectrum (Wolf & Toon 2014). Horizontal resolution of the model is 4° in latitude and 5° in longitude with 40 levels in the vertical direction, and the top of the model is ≈1 hPa. The time step is 30 minutes. Each experiment was run for tens of Earth years to 100 Earth years until the surface and atmosphere reach equilibrium. By default, averages of the last 10 years were used here.

3. Results

3.1. Non-monotonic Dependence of Planetary Climate on pN_2

The planetary climate is a non-monotonous function of $p\mathrm{N}_2$, under a given stellar flux. As shown in Figure 2 and Table 1, the global-mean surface temperature is 278, 266, 265, 278, 297, and 344 K for $p\mathrm{N}_2$ of 0.25, 0.5, 1.0, 2.0, 4.0, and 10.0 bar, respectively. Several competing processes cause the non-monotonicity, including pressure broadening, lapse rate, relative humidity, heat capacity, and clouds.

For a higher $p\mathrm{N}_2$ than 1.0 bar, such as 4.0 bar, the warmer surface mainly results from three responses: stronger pressure broadening (and N_2–N_2 absorption), higher relative humidity, and a lower planetary albedo. As $p\mathrm{N}_2$ is increased, the global-scale "Walker circulation" (with upwelling over the substellar region and downwelling in the rest region) becomes shallower in altitude, weaker in strength (W and V_r winds), and meanwhile the upwelling area becomes wider in horizontal scale and the downwelling area becomes narrower (Figure 2(e)). The reduction of the downwelling area and the weakening of the downwelling strength allow the atmosphere to be more saturated, so the relative humidity increases especially in the upper troposphere (Figure 2(b)). The total relative humidity is 69% and 79% in the cases of 1.0 and 4.0 bar, respectively. So, the atmosphere can hold more water vapor and have a stronger greenhouse effect, warming the surface. Water vapor feedback further increases clear-sky atmospheric greenhouse effect and amplifies the surface warming. The weakening of atmospheric circulation with $p\mathrm{N}_2$ is consistent with the ideal 3D simulations of Kaspi & Showman (2015), Chemke et al. (2016), and Chemke & Kaspi (2017). Note that the mass streamfunction (contour lines in Figure 2(f)) becomes stronger with $p\mathrm{N}_2$ due to the increase in air mass, despite the weaker velocities. The stronger mass streamfunction transports more heat from the dayside to the nightside, reducing the day-to-night thermal contrast (Figure 2(a)).

In the case of 4.0 bar, planetary albedo is 0.38 while it is 0.44 in the case of 1.0 bar (Table 1). This implies that Rayleigh scattering, which increases with $p\mathrm{N}_2$, is not the reason. The planetary albedo on tidally locked planets is mainly from the strong convection and clouds over the substellar region (Figures 2(g) and (h); see also Yang et al. 2013), which weakens the effect of Rayleigh scattering. Moreover, at high temperatures, near-infrared absorption by water vapor also reduces the effect of Rayleigh scattering (Ramirez 2020); as shown in Figure 1(b), planetary albedos under different $p\mathrm{N}_2$ approach a constant value under hot climates in the 1D radiative-convective model without clouds. Therefore, we can say that Rayleigh scattering is unimportant for the inner edge of the habitable zone. The lower planetary albedo in the case of 4.0 bar is related to the reduction of cloud water amount, which exhibits a decreasing trend with $p\mathrm{N}_2$ (Figure 2(g) except the 10.0 bar case). The underlying mechanism is the increase of lapse rate (going closer to dry adiabatic) when $p\mathrm{N}_2$ is increased. Therefore, less condensation occurs in the troposphere. The cloud fraction, determined by the combination of convection mass flux, stratification, and relative humidity (Neale et al. 2010), does not exhibit a clear trend (Figure 2(h)). Because convection and clouds are parameterized in the model, the response of clouds to varying $p\mathrm{N}_2$ may be model dependent; large differences exist in simulating clouds among AGCMs as shown in Yang et al. (2019d) and Fauchez et al. (2020).

The 10.0 bar case exhibits a quite different behavior: the global-scale Walker cell and the convection occur in the levels above 7.0 bar, below which temperature gradients are small even around the terminators and the atmosphere is calm (the rightmost panels in Figure 2); this climate state is similar to that on Venus (Read et al. 2018). In this case, surface temperature differences between the day and night are within 3 K, and the low-level atmosphere shows a counterclockwise (rather than clockwise) circulation. The latter is due to the weakening of convective fluxes with increasing $p\mathrm{N}_2$ (Chemke & Kaspi 2017) and to the cooling effect of the evaporation of precipitating droplets over the substellar region below the level of 7.0 bar (figure not shown), which causes atmospheric downwelling there.

For a lower $p\mathrm{N}_2$ than 1.0 bar, such as 0.25 bar, the relatively warmer surface is mainly from cloud response and lapse rate change. Planetary albedos are 0.40 and 0.44 in the cases of 0.25 and 1.0 bar, respectively. The lower albedo under 0.25 bar is mainly from the smaller cloud fraction in the region between 50° and 80° (in tidally locked coordinates, see the leftmost panels in Figures 2(g) and (h)). This region is dominated by downwelling under $p\mathrm{N}_2 = 0.25$ bar rather than upwelling as that in $p\mathrm{N}_2 = 1.0$ bar, which is related to the expanding trend of the upwelling region with increasing $p\mathrm{N}_2$ as described above. For a lower $p\mathrm{N}_2$, the lapse rate is smaller under a given surface temperature, so that the air temperature aloft is higher (Figure 1(d)) and more vapor can be maintained in the atmosphere (Figure 1(e)), following the Clausius–Clapeyron relation. So, the 0.25 bar case can hold more water vapor in the air, warming the surface. Again, water vapor feedback acts to further amplify the surface warming. The total relative humidity in the 0.25 bar case is also higher than that in the 1.0 bar case but with a much smaller magnitude, 72% versus 69%, which is likely due to the increase of vapor concentration aloft, associated with the reduced lapse rate.

A clear trend is the decreasing of shortwave heating rate with increasing $p\mathrm{N}_2$ (Figure 2(d)). This is due to the increases of heat capacity and lapse rate with $p\mathrm{N}_2$, as described in Section 1 and in Chemke et al. (2016). The effect of heat capacity dominates; for example, vertically integrated water vapor amounts are 64 and 37 kg m^{-2} in the cases of 0.25 and 1.0 bar, respectively, while the total heat capacity of the former is only ≈25% of that in the latter. Another clear trend is the reduction of low-level clouds on the nightside (Figures 2(g) and (h)). These clouds are trapped under the temperature inversion by large-scale circulation. As the circulation shrinks in altitude or completely collapses, these clouds become thinner or disappear. These clouds have no shortwave cooling effect due to the lack of stellar energy deposition on the nightside but have a negative longwave cloud radiation effect (LWCRE), because

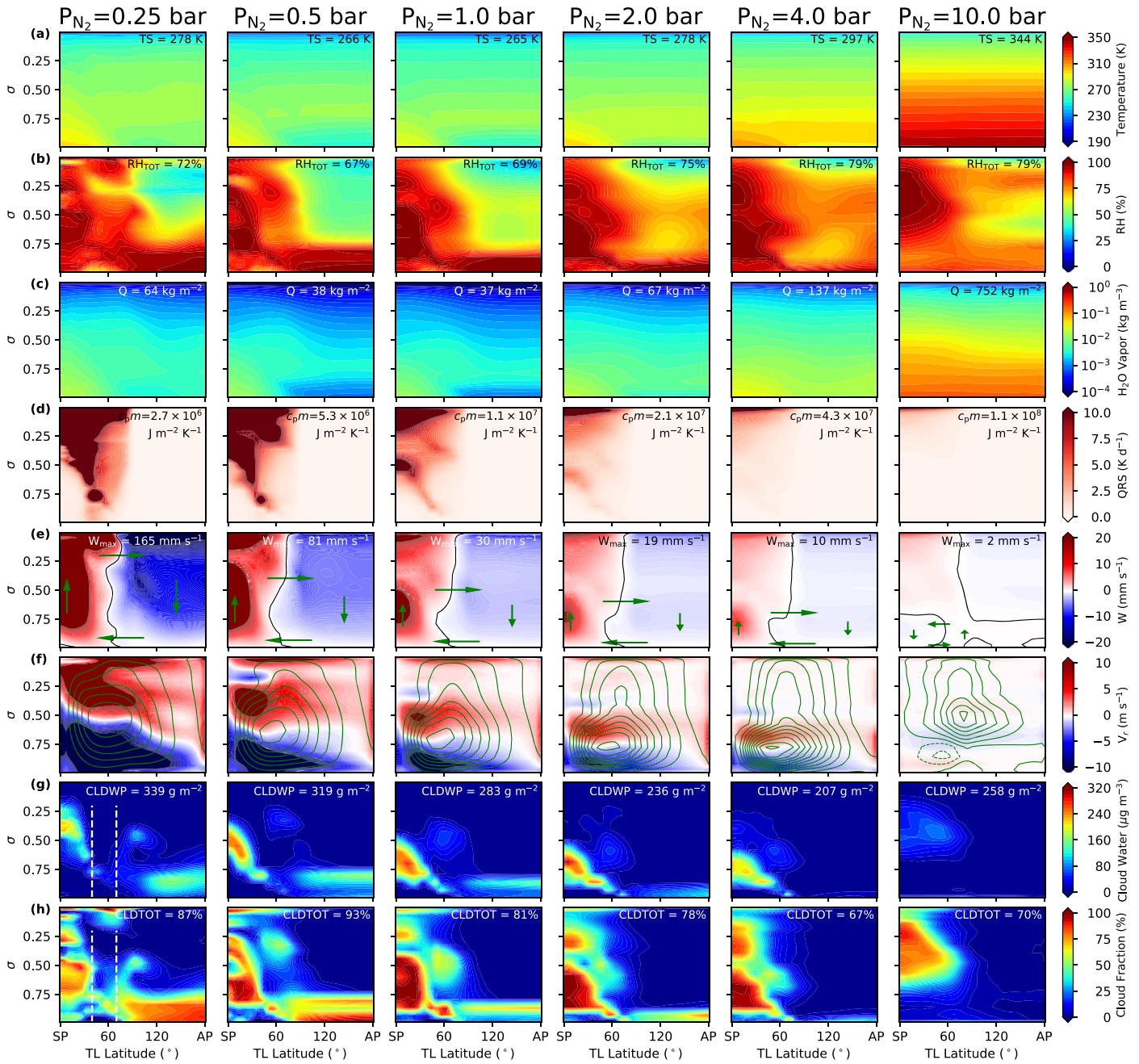

Figure 2. Effects of pN_2 on the climate of a tidally locked aqua-planet. (a) Air temperature, (b) relative humidity (RH), (c) water vapor concentration, (d) shortwave heating rate (QRS), (e) vertical velocity (W, solid line is zero velocity), (f) radial velocity (V_r), (g) cloud water content, and (h) cloud fraction in tidally locked (TL) coordinates, for pN_2 of 0.25, 0.5, 1.0, 2.0, 4.0, and 10.0 bar from the left to right columns. The substellar point (SP) and antistellar point (AP) are at 0° and 180°, respectively. The contour lines in (f) are mass streamfunction with intervals of 10^{11} kg s^{-1} (solid lines: clockwise; dashed lines: counterclockwise). The vertical dashed lines in (g) and (h) mask the region where the cloud fraction is relatively low. The numbers in the right corner of each panel is global-mean surface temperature in (a), total relative humidity in (b) (defined as the percentage of water vapor by mass contained in the whole atmosphere compared with the vapor mass that the atmosphere could theoretically hold if saturated everywhere, following Wolf & Toon 2015), vertically integrated water vapor amount in (c), total atmospheric heat capacity in (d) (defined as C_{pm} where C_p is the specific heat capacity and m is the vertically integrated air mass per unit area), maximum vertical velocity below $\sigma = 0.1$ in (e), vertically integrated cloud water path in (g), and total cloud water fraction in (h) (assuming maximum–random overlap). The stellar flux is 1700 W m^{-2}, star temperature is 3700 K, and rotation period is 60 Earth days in all of these experiments.

they are close to the temperature inversion. If OHT is included in the simulations, the temperature inversion will be weaker or even disappear, and the value of LWCRE will turn positive (see Figure 2 in Yang et al. 2019b).

Table 1 exhibits that energy balance of the system is negative with magnitudes of 1–4 W m^{-2}, especially in the relatively cooler experiments. This energy imbalance is mainly due to continuous growths of surface snow and sea ice, especially on the nightside (figures not shown). The continued growth of sea ice is due to the fact that neither geothermal heat flux at the ocean bottom nor OHT from the open ocean to the ice beneath is considered in the simulations. Without OHT, the ice will grow to thousands of meters (Menou 2013). If OHT is included, the ice will be limited to several or tens of meters (Hu & Yang 2014; Yang et al. 2014b). However, the snow depth and ice thickness do not influence the surface temperature

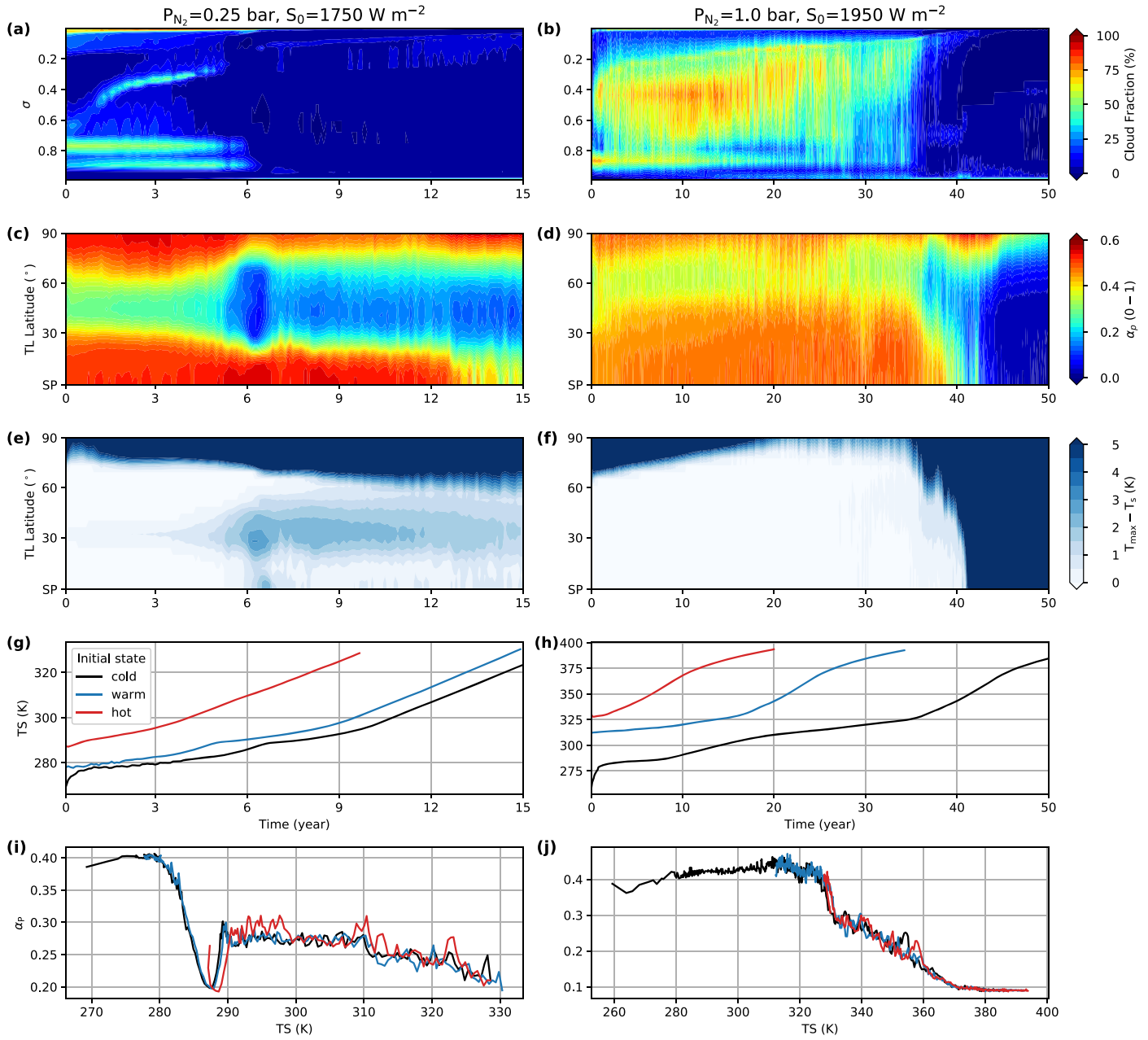

Figure 3. The trigger of runaway greenhouse (a)–(f) and its insensitivity to initial condition (g)–(j), in the slowly rotating experiments. (a)–(f) Time evolution of cloud fraction in σ coordinates (a) and (b) (averages between 0° and 60°), planetary albedo (c) and (d), and temperature inversion (e) and (f) (defined as maximum air temperature minus the corresponding surface temperature) in tidally locked coordinates. SP is the substellar point. (g)–(j) The evolution of global-mean surface temperature as a function of time (g) and (h) and the evolution of planetary albedo as a function of the global-mean surface temperature (i) and (j) in the experiments using different initial states: cold, warm, and hot. Left panels are for the experiments of pN_2 of 0.25 bar and stellar flux of 1750 W m^{-2} and right panels for 1.0 bar and 1950 W m^{-2}. The cases of 4.0 bar are similar to the 1.0 bar cases and so they are not shown for clarity. These experiments suggest that the trigger of the runaway greenhouse state is associated with the temperature inversion onset and cloud collapse, and it is insensitive to the initial condition.

significantly (within 1.5 K in global mean); this is because a small thickness of snow or sea ice is able to have a strong isolation effect between the ocean and the atmosphere and to have a relatively high, saturated surface albedo in the regions under stellar deposition.

3.2. The Inner Edge of the Habitable Zone

For the inner edge of the habitable zone, we focus on three levels of pN_2, 0.25, 1.0, and 4.0 bar. The stellar flux thresholds for the onset of the runaway greenhouse on a slowly rotating aqua-planet (60 earth days) are 1700–1750, 1900–1950, and 1750–1800 W m^{-2}, respectively. This again exhibits a non-monotonic feature. For a rapidly rotating planet, the stellar flux thresholds are smaller, 1300–1350, 1350–1400, and 1400–1450 W m^{-2}, respectively. The differences are smaller for the rapidly rotating aqua-planet; this is primarily due to the smaller cloud albedo (Table 1).

In all the experiments, the onset of the runaway greenhouse is related to the appearance of temperature inversion on the dayside, away from the terminators (Figure 3), followed by the collapse of convection and clouds, similar to that found in Wolf & Toon (2015), Popp et al. (2015, 2016), and Kopparapu et al. (2017). As shown in Figures 3(a), (c), and (e), in the

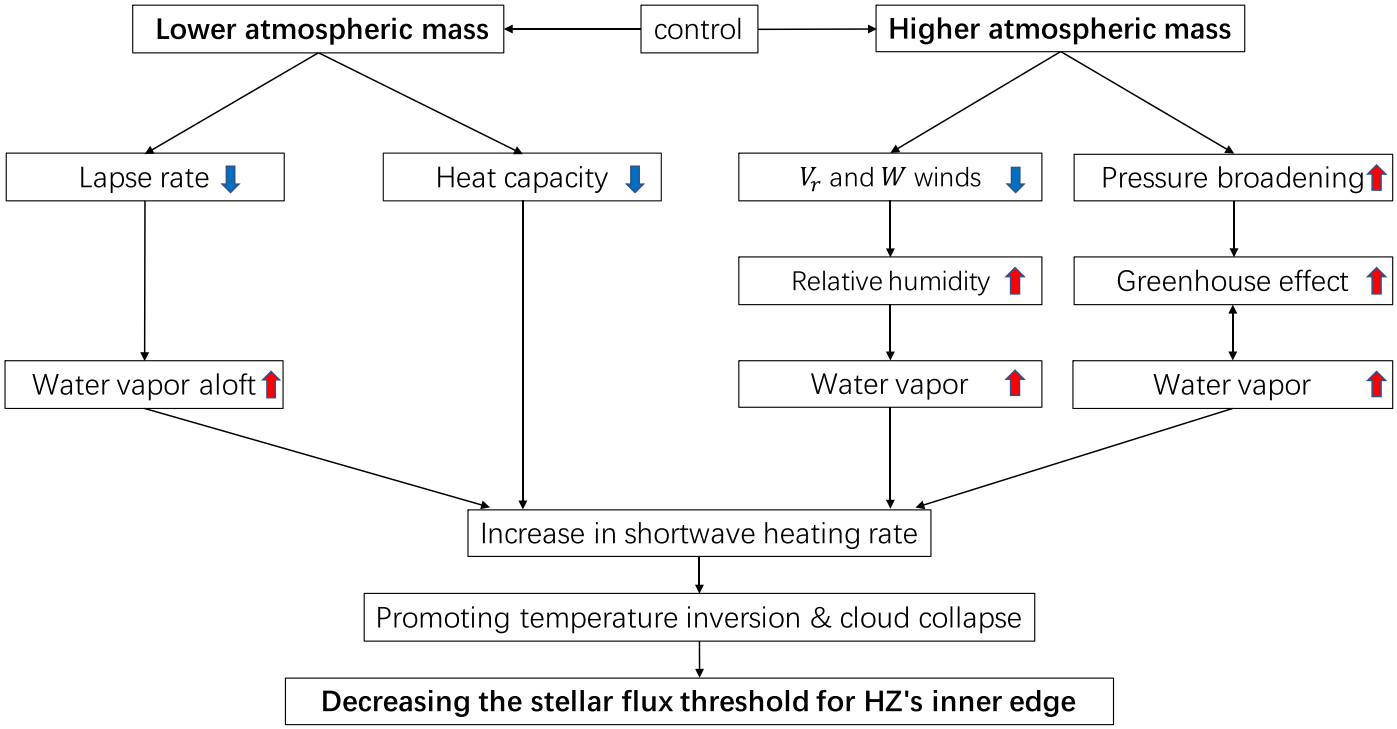

Figure 4. Schematic illustration for the effects of varying N_2 partial pressure on the inner edge of the habitable zone. The inner edge is defined based on runaway greenhouse. Five factors, pressure broadening, heat capacity, lapse rate, relative humidity, and clouds, make the problem much more complex than that found in 1D models and cause the stellar flux threshold for the runaway greenhouse onset to be a non-monotonic function of $p\mathrm{N}_2$.

experiment of 0.25 bar and 1750 W m^{-2}, temperature inversion and cloud collapse occur in the sixth model year within the region of 30°–60° (in tidally locked coordinates); after that, the planetary albedo decreases dramatically. So, the global-mean shortwave absorption becomes larger than the outgoing longwave radiation, and the system suddenly enters a runaway greenhouse state. Similar phenomena occur in the experiment of 1.0 bar and 1950 W m^{-2} (Figures 3(b), (d), and (f)).

Sensitivity tests show that the onsets of the temperature inversion and cloud collapse do not depend on the initial condition (Figures 3(g)–(j)). When the model is initialized from different surface temperatures, all the experiments enter runaway greenhouse and the curves of planetary albedo (as well as energy imbalance and outgoing longwave radiation; not shown) as a function of global-mean surface temperature roughly follow the same line (Figures 3(i)–(j)).

The onset of the temperature inversion is due to strong shortwave absorption by water vapor when the low-level atmosphere has already become optical thick in thermal radiation (Wordsworth & Pierrehumbert 2013; Wolf & Toon 2015). At high temperatures, water vapor strongly absorbs stellar radiation especially in the near-infrared wavelengths. For $p\mathrm{N}_2 = 0.25$ bar, the system enters runaway greenhouse at a lower stellar flux threshold than that of 1.0 bar $p\mathrm{N}_2$. This is mainly due to the effects of lapse rate and heat capacity as described above. More water vapor can be held in the atmosphere and the heat capacity is smaller, causing a larger shortwave heating rate, so the onset of the temperature inversion occurs at a lower surface temperature (≈280 versus 320 K in global mean; see Figures 3(i)–(j)). For $p\mathrm{N}_2 = 4.0$ bar, the system also enters runaway greenhouse at a lower stellar flux than that of 1.0 bar. This is due to the increases of relative humidity (as discussed in Section 3.1) and of water vapor concentration; the latter is associated with the combined effect of pressure broadening and water vapor feedback. As $p\mathrm{N}_2$ is increased, the greenhouse effect becomes stronger due to pressure broadening, so surface and air temperatures increase and then more water vapor can be held in the atmosphere. Because water vapor is a greenhouse gas, the greenhouse effect further raises, which leads to even greater surface and air warming and larger shortwave heating rate, promoting the onsets of the temperature inversion and cloud collapse.

4. Summary

The 3D global climate model ExoCAM was employed to investigate the effects of varying $p\mathrm{N}_2$ on the stellar flux threshold for the onset of the runaway greenhouse state on tidally locked rocky planets around M dwarfs. Comparing previous studies on this problem using 1D radiative-convective models (Nakajima et al. 1992; Kasting et al. 1993; Goldblatt et al. 2009; Kopparapu et al. 2014; Ramirez 2020), the main new findings are summarized as follows and schematically shown in Figure 4.

(1) The global-mean surface temperature and the stellar flux threshold for the runaway greenhouse onset are non-monotonous functions of $p\mathrm{N}_2$, due to the competing effects of five different processes, including clouds, pressure broadening, heat capacity, lapse rate, and relative humidity. Rayleigh scattering is unimportant for the inner edge, due to that cloud albedo and near-infrared absorption by water vapor are effective in masking the effect of Rayleigh scattering.

(2) Lapse rate and water vapor aloft decrease with increasing $p\mathrm{N}_2$ and atmospheric heat capacity increases with $p\mathrm{N}_2$, so shortwave heating rate by water vapor decreases with $p\mathrm{N}_2$

under a given surface temperature. These act to delay the onsets of temperature inversion and runaway greenhouse.

(3) The effects of pressure broadening and N_2–N_2 absorption increase with pN_2; this warms the surface and increases water vapor concentration. Water vapor feedback further amplifies the warming. These promote the onsets of temperature inversion and runaway greenhouse.

(4) The atmospheric circulation (W and V_r winds) is a clear monotonically decreasing function of pN_2, although the horizontal energy transport increases with pN_2. This can influence the relative humidity. But no clear trend is found in cloud fraction or cloud albedo on the dayside, due to complex moist processes and the interactions between them and atmospheric circulation, although the nightside clouds exhibit a clear decreasing trend with pN_2.

(5) Finally, for the inner edge, the magnitude for the effect of varying pN_2 is within 13% under the parameters we examined, which is comparable to that of varying planetary radius and gravity (within ≈9%; Yang et al. 2019a) and of the uncertainty in pure water vapor radiation transfer (within ≈10%; Yang et al. 2016), but smaller than that of the uncertainty in the cloud scheme (within ≈50%; Bin et al. 2018) and of varying rotation period and stellar spectrum (within ≈70%; Kopparapu et al. 2017).

Future work is required to investigate tidally locked planets in spin–orbit resonance states like Mercury and rapidly rotating planets like Earth. For these planets, atmospheric circulation and cloud distribution are different from those of 1:1 tidally locked planets (Yang et al. 2014a; Wang et al. 2016; Salameh et al. 2018); this can strongly influence the trend of the effect of pN_2 on the inner edge, following the analyses above. Finally, we note that atmospheric masses or N_2 pressures on exoplanets could be inferred from the observations of phase curves (Koll & Abbot 2015; Koll 2019; Kreidberg et al. 2019), emission and transmission spectra (especially the N_2–N_2 absorption in 4.15 μm and in the wings of the 4.3 μm CO_2 band; Schwieterman et al. 2015), or Raman scattering (Oklopčić et al. 2016).

We are grateful to Eric Wolf for the release of the model ExoCAM and to Ravi Kumar Kopparapu for his helpful comments and suggestions. J.Y. acknowledges support from the National Natural Science Foundation of China (NSFC) under grant 41675071.

Software: ExoRT (https://github.com/storyofthewolf/ExoRT), ExoCAM (https://github.com/storyofthewolf/ExoCAM), Tidally Locked Coordinates (https://github.com/ddbkoll/tidally-locked-coordinates).

ORCID iDs

Yixiao Zhang https://orcid.org/0000-0001-6194-760X
Jun Yang https://orcid.org/0000-0001-6031-2485

References

Allard, F., Allard, N. F., Homeier, D., et al. 2007, A&A, 474, L21
Bin, J., Tian, F., & Liu, L. 2018, E&PSL, 492, 121
Charnay, B., Forget, F., Wordsworth, R., et al. 2013, JGRD, 118, 10414
Chemke, R., & Kaspi, Y. 2017, ApJ, 845, 1
Chemke, R., Kaspi, Y., & Halevy, I. 2016, GeoRL, 43, 11414
Fauchez, T. J., Turbet, M., Wolf, E. T., et al. 2020, GMD, 13, 707
Fujii, Y., Del Genio, A. D., & Amundsen, D. S. 2017, ApJ, 848, 100
Goldblatt, C., Claire, M. W., Lenton, T. M., et al. 2009, NatGe, 2, 891
Goldblatt, C., Robinson, T. D., Zahnle, K. J., & Crisp, D. 2013, NatGe, 6, 661
Hu, R., & Diaz, H. D. 2019, ApJ, 886, 126
Hu, Y., & Yang, J. 2014, PNAS, 111, 629
Ingersoll, A. 2013, Planetary Climates, Vol. 9 (Princeton, NJ: Princeton Univ. Press)
Johnson, B., & Goldblatt, C. 2015, ESRv, 148, 150
Kaspi, Y., & Showman, A. P. 2015, ApJ, 804, 60
Kasting, J. F., Kopparapu, R., Ramirez, R. M., & Harman, C. E. 2014, PNAS, 111, 12641
Kasting, J. F., Whitmire, D. P., & Reynolds, R. T. 1993, Icar, 101, 108
Keles, E., Grenfell, J. L., Godolt, M., Stracke, B., & Rauer, H. 2018, AsBio, 18, 116
Koll, D. D. 2019, arXiv:1907.13145
Koll, D. D., & Abbot, D. S. 2015, ApJ, 802, 21
Komacek, T. D., & Abbot, D. S. 2019, ApJ, 871, 245
Kopparapu, R. K., Ramirez, R. M., SchottelKotte, J., et al. 2014, ApJL, 787, L29
Kopparapu, R. k., Wolf, E. T., Arney, G., et al. 2017, ApJ, 845, 5
Kopparapu, R. k., Wolf, E. T., Haqq-Misra, J., et al. 2016, ApJ, 819, 84
Kreidberg, L., Koll, D. D., Morley, C., et al. 2019, Natur, 573, 87
Leconte, J., Forget, F., Charnay, B., Wordsworth, R., & Pottier, A. 2013, Natur, 504, 268
Marty, B., Zimmermann, L., Pujol, M., Burgess, R., & Philippot, P. 2013, Sci, 342, 101
Menou, K. 2013, ApJ, 774, 51
Merlis, T. M., & Schneider, T. 2010, JAMES, 2, 13
Moore, K., & Cowan, N. B. 2020, MNRAS, 496, 3786
Nakajima, S., Hayashi, Y.-Y., & Abe, Y. 1992, JAtS, 49, 2256
Neale, R. B., Chen, C.-C., Gettelman, A., et al. 2010, NCAR Tech. Note NCAR/TN-486+STR, https://www.ccsm.ucar.edu/models/ccsm4.0/cam/docs/description/cam4_desc.pdf
Noda, S., Ishiwatari, M., Nakajima, K., et al. 2017, Icar, 282, 1
Oklopčić, A., Hirata, C. M., & Heng, K. 2016, ApJ, 832, 30
Pierrehumbert, R. T. 2010, Principles of Planetary Climate (Cambridge: Cambridge Univ. Press)
Popp, M., Schmidt, H., & Marotzke, J. 2015, JAtS, 72, 452
Popp, M., Schmidt, H., & Marotzke, J. 2016, NatCo, 7, 10627
Ramirez, R. M. 2020, MNRAS, 494, 259
Read, P. L., Lewis, S. R., & Vallis, G. K. 2018, in Handbook of Exoplanets, ed. H. Deeg & J. Belmonte (Cham: Springer), 50
Salameh, J., Popp, M., & Marotzke, J. 2018, ClDy, 50, 2395
Schwieterman, E. W., Robinson, T. D., Meadows, V. S., Misra, A., & Domagal-Goldman, S. 2015, ApJ, 810, 57
Selsis, F., Kasting, J. F., Levrard, B., et al. 2007, A&A, 476, 1373
Shields, A. L., Ballard, S., & Johnson, J. A. 2016, PhR, 663, 1
Som, S. M., Buick, R., Hagadorn, J. W., et al. 2016, NatGe, 9, 448
Vladilo, G., Murante, G., Silva, L., et al. 2013, ApJ, 767, 65
von Paris, P., Grenfell, J. L., Rauer, H., & Stock, J. W. 2013, P&SS, 82, 149
Wang, Y., Liu, Y., Tian, F., et al. 2016, ApJL, 823, L20
Way, M. J., Del Genio, A. D., Aleinov, I., et al. 2018, ApJS, 239, 24
Way, M. J., Del Genio, A. D., Kiang, N. Y., et al. 2016, GeoRL, 43, 8376
Wolf, E., & Toon, O. 2014, AsBio, 14, 241
Wolf, E., & Toon, O. 2015, JGRD, 120, 5775
Wolf, E. T. 2017, ApJL, 839, L1
Wolf, E. T., Shields, A. L., Kopparapu, R. K., Haqq-Misra, J., & Toon, O. B. 2017, ApJ, 837, 107
Wordsworth, R. 2015, ApJ, 806, 180
Wordsworth, R. 2016, E&PSL, 447, 103
Wordsworth, R., & Pierrehumbert, R. 2014, ApJL, 785, L20
Wordsworth, R., & Pierrehumbert, R. T. 2013, ApJ, 778, 154
Yang, H., Komacek, T. D., & Abbot, D. S. 2019a, ApJL, 876, L27
Yang, J., Abbot, D. S., Koll, D. D., Hu, Y., & Showman, A. P. 2019b, ApJ, 871, 29
Yang, J., Boué, G., Fabrycky, D. C., & Abbot, D. S. 2014a, ApJL, 787, L2
Yang, J., Cowan, N. B., & Abbot, D. S. 2013, ApJL, 771, L45
Yang, J., Leconte, J., Wolf, E. T., et al. 2016, ApJ, 826, 222
Yang, J., Leconte, J., Wolf, E. T., et al. 2019c, ApJ, 875, 46
Yang, J., Leconte, J., Wolf, E. T., et al. 2019d, ApJ, 875, 46
Yang, J., Liu, Y., Hu, Y., & Abbot, D. S. 2014b, ApJL, 796, L22
Zsom, A., Seager, S., De Wit, J., & Stamenković, V. 2013, ApJ, 778, 109